
Figures and figure supplements

Two opposite voltage-dependent currents control the unusual early development pattern of embryonic Renshaw cell electrical activity

Juliette Boeri et al

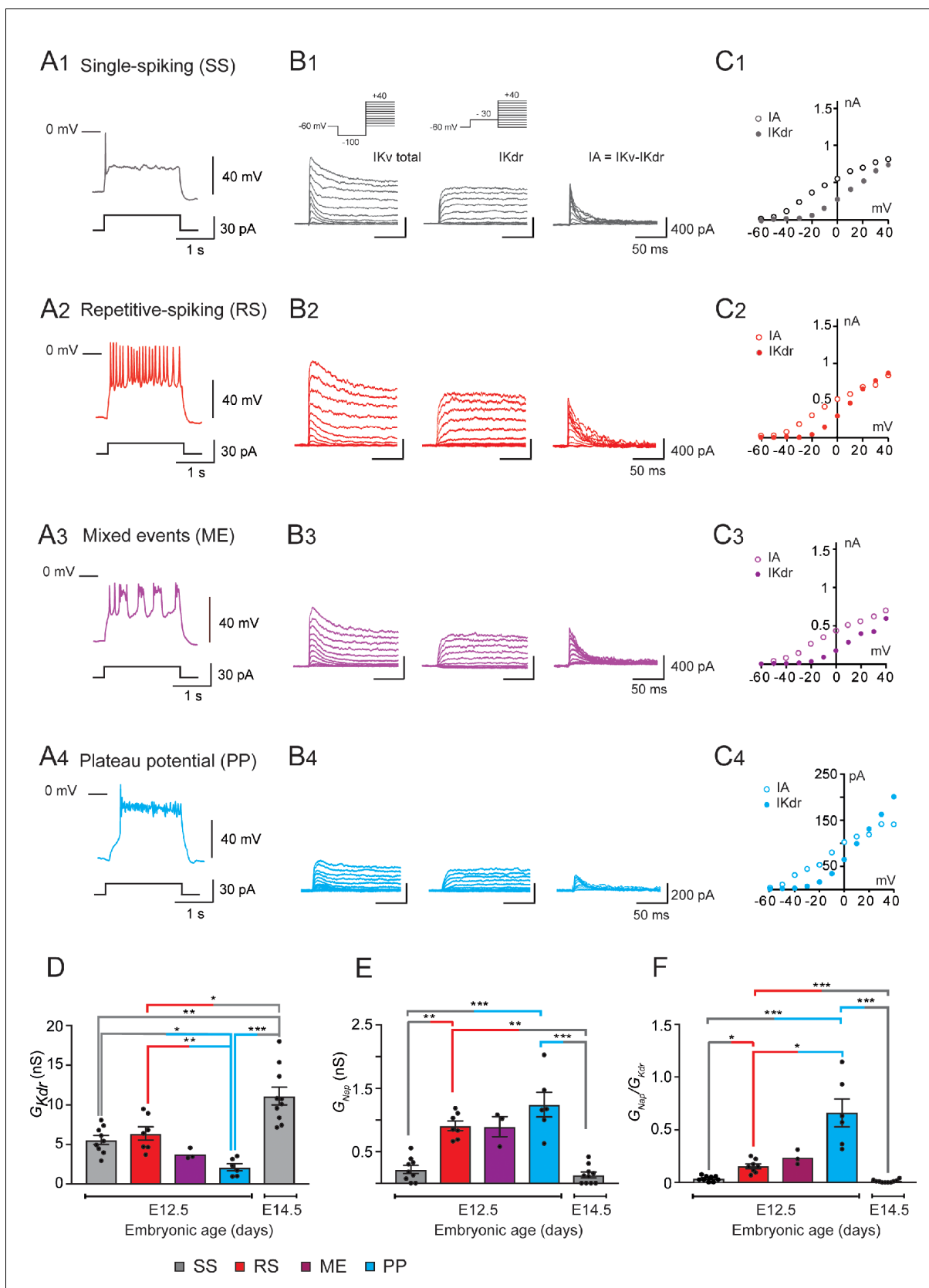


Figure 1. G_{Kdr} and G_{Nap} in embryonic $V1^R$ at E12.5 and E14.5. (A) Representative traces of voltage responses showing single spiking (SS) activity in E12.5 SS $V1^R$ (A1), repetitive action potential firing in repetitive spiking (RS) $V1^R$ (A2), mixed plateau potential activity (PP) and repetitive action potential (A3). (B) Representative current traces showing total current (B1), delayed rectifier current (I_{Kdr}) (B2), and subtracted current ($I_A = I_{total} - I_{Kdr}$) (B3) for each activity type. (C) Current-voltage ($I-V$) plots for I_A (open circles) and I_{Kdr} (filled circles) for each activity type. (D) G_{Kdr} and G_{Nap} for each activity type at E12.5 and E14.5. (E) G_{Nap} for each activity type at E12.5 and E14.5. (F) G_{Nap}/G_{Kdr} for each activity type at E12.5 and E14.5. Statistical significance is indicated by asterisks (*, **, ***, ****).

Figure 1 continued

firing in mixed event (ME) V1^R (A3), and PP activity in PP V1^R (A4). (B) Representative examples of the total outward K⁺ currents (IKV total) obtained from V_H = −100 mV (left traces), of I_{Kdr} (V_H = −30 mV, middle traces), and of isolated I_A (left traces) recorded at E12.5 in SS V1^R (B1), RS V1^R (B2), ME V1^R (B3), and PP V1^R (B4). Voltage-dependent potassium currents were evoked in response to 10 mV membrane potential steps (200 ms) from −100 or from −30 mV to +40 mV (10 s interval between pulses). V1^R were voltage clamped at V_H = −60 mV. A prepulse of −40 mV (300 ms) was applied to activate both I_A and I_{Kdr}. I_{Kdr} was isolated by applying a prepulse of −30 mV (300 ms) to inactivate I_A (B1 inset). I_A was isolated by subtracting step-by-step the currents obtained using a prepulse of −30 mV (V_H = −30 mV) from the currents obtained using a prepulse of −40 mV (V_H = −100 mV). (C) Current-voltage relationship (*I* – *V* curves) of I_{Kdr} (filled circles) and of I_A (open circles) recorded in SS V1^R (C1), RS V1^R (C2), ME V1^R (C3), and PP V1^R (C4). *I* – *V* curves were obtained from currents shown in (B1), (B2), (B3), and (B4). Note that *I* – *V* curves are similar between SS V1^R, RS V1^R, ME V1^R, and PP V1^R. (D) Bar graph showing maximal G_{Kdr} value (Max G_{Kdr}) in SS V1^R at E12.5 (n = 9; N = 9; gray bar) and at E14.5 (n = 10; N = 10 gray bar), and in RS V1^R (n = 7; N = 7; red bar), ME V1^R (n = 3; N = 3 purple bar), and PP V1^R at E12.5 (n = 7; N = 7 blue bar) was calculated from I_{Kdr} at V_H = +20 mV, assuming a K⁺ equilibrium potential of −96 mV. There is no significant difference in G_{Kdr} between SS V1^R and RS V1^R, while G_{Kdr} is significantly smaller in PP V1^R as compared to G_{Kdr}. SS V1^R and RS V1^R was significantly higher in SS V1^R at E14.5 than in SS V1^R, RS V1^R, and PP V1^R at E12.5 (Kruskal–Wallis test p<0.0001; SS V1^R versus RS V1^R at E12.5, p=0.5864; SS V1^R versus PP V1^R at E12.5, p=0.0243; RS V1^R versus PP V1^R at E12.5, p=0.0086; E14.5 SS V1^R versus E12.5 SS V1^R, p=0.0048; E14.5 SS V1^R versus E12.5 RS V1^R, p=0.0384, E14.5 SS V1^R versus E12.5 PP V1^R, p<0.0001). The increase in G_{Kdr} density between E12.5 and E14.5 is likely to be due to the increase in neuronal size (input capacitance; Figure 2A). Indeed, there was no significant difference (Mann–Whitney test, p=0.133) in G_{Nap} between SS V1^R at E12.5 (n = 9; N = 9 gray bar) and at E14.5 (n = 10; N = 10 gray bar). (E) Bar graph showing the maximal Max G_{Nap} value (G_{Nap}) in SS V1^R at E12.5 (n = 9; N = 9 gray bar) and E14.5 (n = 10; N = 10 gray bar), and in RS V1^R (n = 8; N = 8 red bar), ME V1^R (n = 3; N = 3 purple bar), and PP V1^R (n = 6; N = 6 blue bar) at E12.5. Max I_{Nap} was calculated from maximal G_{Nap} value measured on current evoked by assuming a Na⁺ equilibrium potential of +60 mV. There was no difference in G_{Nap} between RS V1^R and PP V1^R. On the contrary, G_{Nap} measured in SS V1^R at E12.5 or at E14.5 was significantly smaller as compared to G_{Nap} measured at E12.5 in RS V1^R or in PP V1^R measured at E12.5 and E14.5 in SS V1^R were not significantly different (Kruskal–Wallis test p<0.0001; E12.5 SS V1^R versus E12.5 RS V1^R, p=0.0034; E12.5 SS V1^R versus E12.5 PP V1^R, p=0.0006; E12.5 RS V1^R versus E12.5 PP V1^R, p=0.5494; E14.5 SS V1^R versus E12.5 SS V1^R, p=0.5896; E14.5 SS V1^R versus E12.5 RS V1^R, p=0.0005; E14.5 SS V1^R versus E12.5 PP V1^R, p<0.0001). (F) Histograms showing the G_{Kdr} / G_{Nap} ratio in SS V1^R at E12.5 (n = 9; gray bar) and E14.5 (n = 10; green bar) and in RS V1^R (n = 8; red bar), ME V1^R (n = 3; purple bar), and PP V1^R (n = 6; blue bar) at E12.5. Note that the G_{Kdr} / G_{Nap} ratio differs significantly between SS V1^R, RS V1^R, and PP V1^R at E12.5, while it is not different between SS V1^R recorded at E12.5 and at E14.5 (Kruskal–Wallis test p<0.0001; SS V1^R versus RS V1^R at E12.5, p=0.0367; SS V1^R versus PP V1^R at E12.5, p<0.0001; RS V1^R versus PP V1^R at E12.5, p=0.0159; E14.5 SS V1^R versus E12.5 SS V1^R, p=0.2319; E14.5 SS V1^R versus E12.5 RS V1^R, p=0.0017; E14.5 SS V1^R versus E12.5 PP V1^R, p<0.0001). Data shown in (A) and (B) were used to calculate G_{Kdr}/C_{in} ratio shown in (C) (*p<0.05, **p<0.01, ***p<0.001).

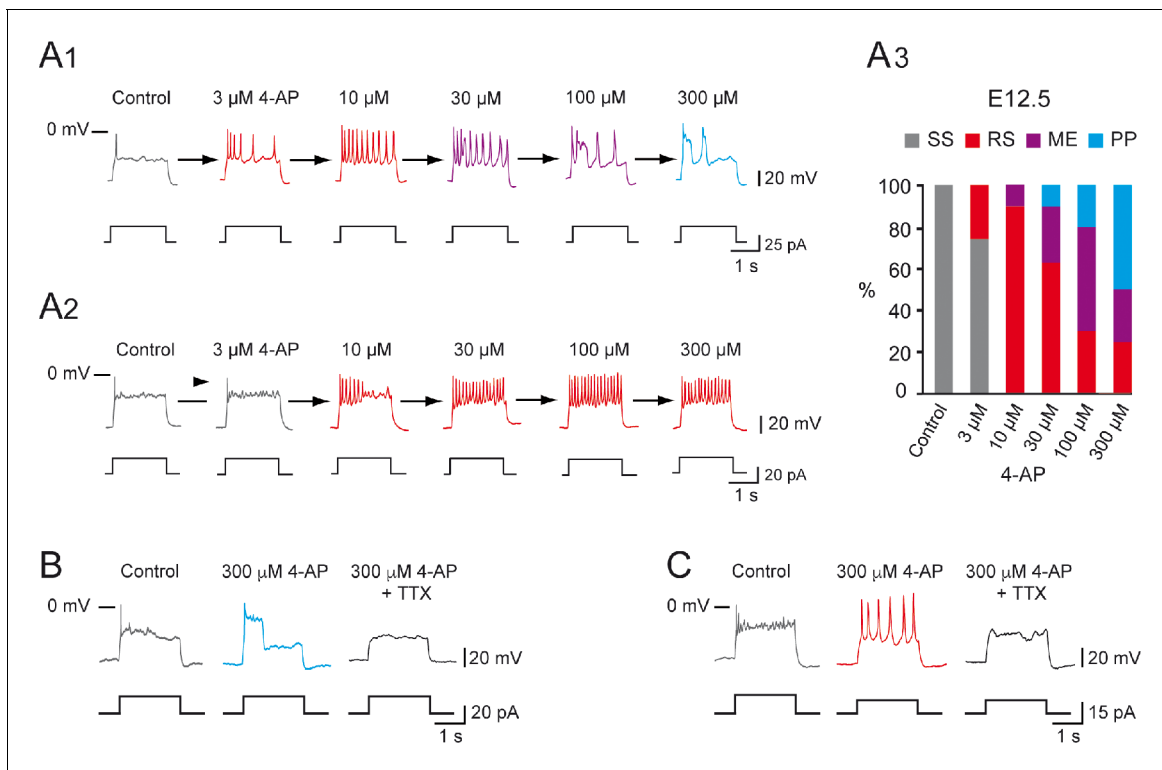


Figure 2. Increasing 4-aminopyridine (4-AP) concentration changed the firing pattern of single spiking (SS) embryonic V1^R recorded at E12.5. The firing pattern of embryonic V1^R was evoked by 2 s suprathreshold depolarizing current steps. **(A)** Representative traces showing examples of the effect of increasing concentration of 4-AP (from 3 to 300 μ M) on the firing pattern of a SS V1^R recorded at E12.5. Note that in **(A1)** increasing 4-AP concentration converted SS (gray trace) to repetitive spiking (red trace), repetitive spiking to a mixed event pattern (purple trace), and mixed events to plateau potential (blue trace). **(A2)** Example of SS V1^R in which increasing 4-AP concentration converted SS to repetitive spiking only. **(A3)** Bar plots showing the change in the firing pattern of SS V1^R according to 4-AP concentrations (control $n = 10$; $N = 10$, 3 μ M 4-AP $n = 8$; $N = 8$, 10 μ M 4-AP $n = 10$; $N = 10$, 30 μ M 4-AP $n = 10$; $N = 10$, 100 μ M 4-AP $n = 10$; $N = 10$, 300 μ M 4-AP $n = 8$; $N = 8$). **(B)** Representative traces showing the effect of 0.5 μ M tetrodotoxin (TTX) on a plateau potential evoked in a SS V1^R in the presence of 300 μ M 4-AP. **(C)** Representative traces showing the effect of 0.5 μ M TTX on repetitive action potential firing evoked in a SS V1^R in the presence of 300 μ M 4-AP. In both cases, the application of TTX fully blocked the responses evoked in the presence of 4-AP, indicating that they were underlain by the activation of voltage-gated Na⁺ channels.

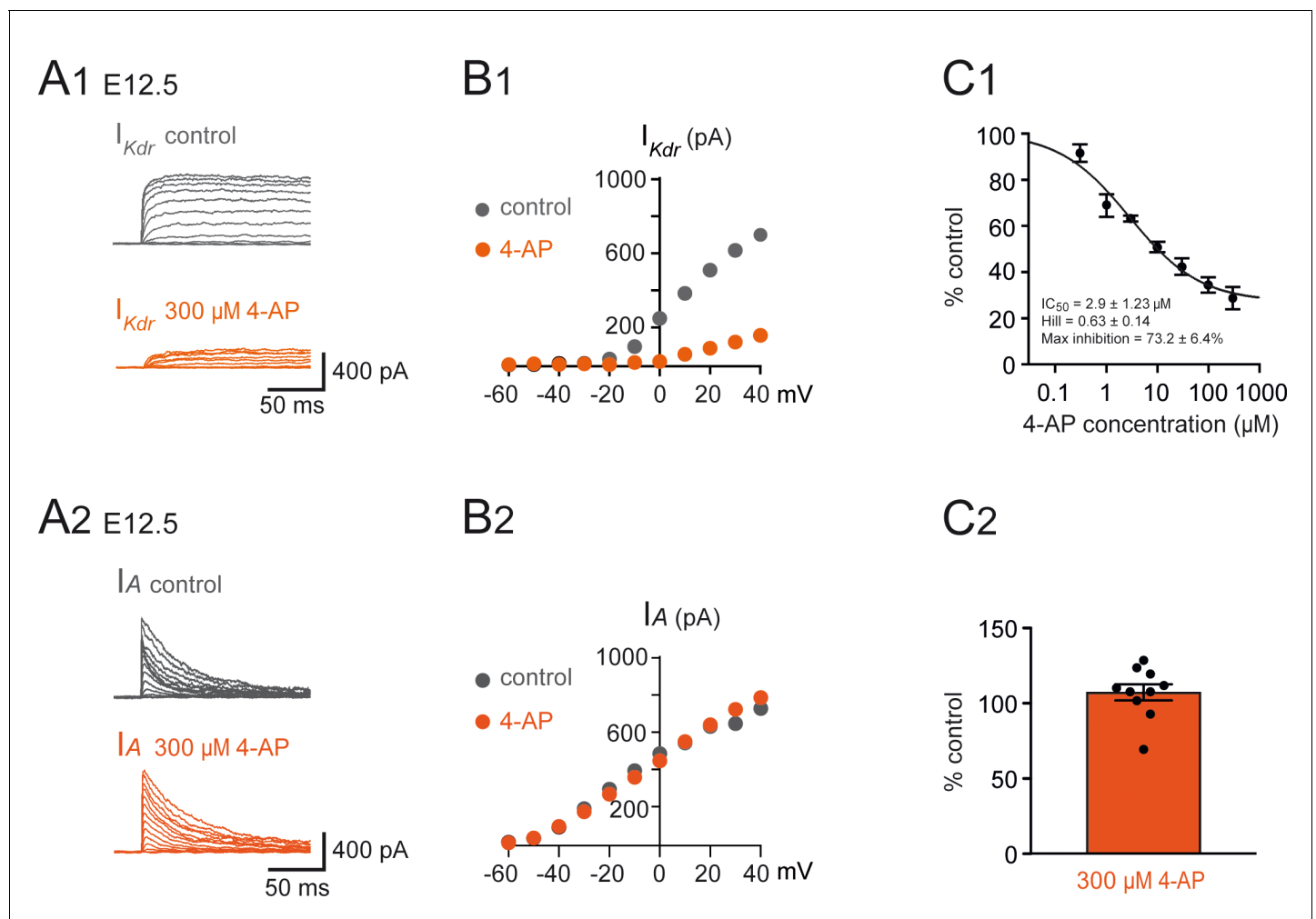


Figure 2—figure supplement 1. Effect of 4-aminopiridine (4-AP) on I_{Kdr} and I_A in embryonic $V1^R$. (A1) Example of voltage-dependent potassium currents evoked in response to 10 mV membrane potential steps (200 ms) from -100 mV or from -30 mV to $+40$ mV (10 s interval between pulses). $V1^R$ were voltage clamped at $V_H = -60$ mV. A prepulse of -40 mV (300 ms) was applied to activate both I_A and I_{Kdr} . I_{Kdr} was evoked in response to 10 mV membrane potential steps (200 ms) from -100 mV to $+40$ mV. $V1^R$ were voltage clamped at $V_H = -60$ mV. A prepulse of 30 mV ($V_H = -30$ mV) was applied to isolate I_{Kdr} . (A1) Representative example of the effect of 300 μ M 4-AP application on I_{Kdr} recorded from embryonic $V1^R$ at E12.5. (B1) Curves showing current-voltage relationships of I_{Kdr} in control and in the presence of 300 μ M 4-AP. Measurements were performed on traces shown in (A1). (C1) Dose-response relationship of 4-AP-evoked I_{Kdr} inhibition (mean + SE). Data were normalized to I_{Kdr} amplitude measured in the absence of 4-AP ($V_H = 40$ mV) and fitted as explained in Materials and methods. Note that 4-AP IC_{50} is in μ M range (2.9 μ M). 0.3 μ M 4-AP $n = 3$; $N = 3$, 1 μ M 4-AP $n = 3$; $N = 3$, 3 μ M 4-AP $n = 9$; $N = 9$, 10 μ M 4-AP $n = 13$; $N = 13$, 30 μ M 4-AP $n = 7$; $N = 7$, 100 μ M 4-AP $n = 7$; $N = 7$, 300 μ M 4-AP $n = 7$; $N = 7$. (A2) Representative example of the effect of 300 μ M 4-AP on I_A in $V1^R$ recorded at E12.5. (B2) I_A Current-voltage ($I - V$) relationship in control conditions and in the presence of 300 μ M 4-AP. The $I - V$ curves were obtained from the traces shown in (A1). (C2) Bar graph showing the percentage of I_A block elicited by 4-AP. Note that 4-AP did not significantly block I_A (Wilcoxon test $p = 0.065$, $n = 10$).

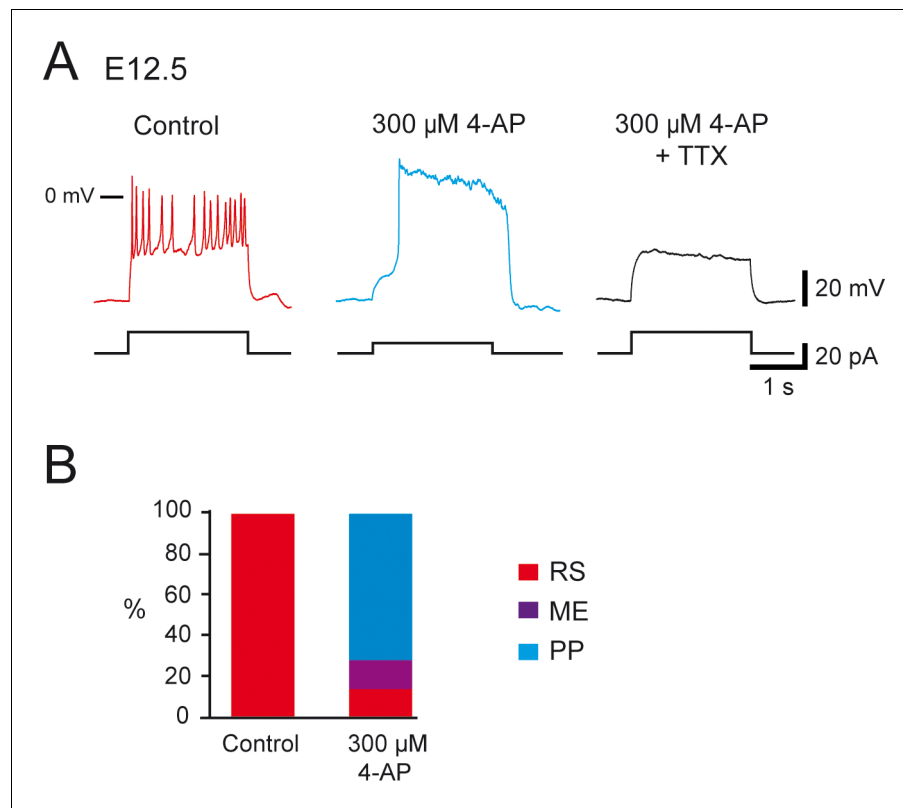


Figure 2—figure supplement 2. Effect of 4-aminopyridine (4-AP) application in repetitively spiking (RS) $V1^R$ at E12.5. **(A)** Representative traces showing the effect of 4-AP application (300 μ M) on RS $V1^R$ at E12.5. Note that plateau potential (PP) activity evoked in the presence of 4-AP (middle trace) was blocked by 0.5 μ M tetrodotoxin (TTX) (right trace). **(B)** Bar plots showing the changes in the firing pattern of RS $V1^R$ evoked by 300 μ M 4-AP application ($n = 14$). 4-AP application evoked a PP in 71.4% of the recorded neurons (10/14) and mixed events (ME) in 14.3% of the recorded neurons (2/14). The excitability pattern was not modified in two neurons. RS $V1^R$ (red), ME $V1^R$ (purple), and PP $V1^R$ (blue).

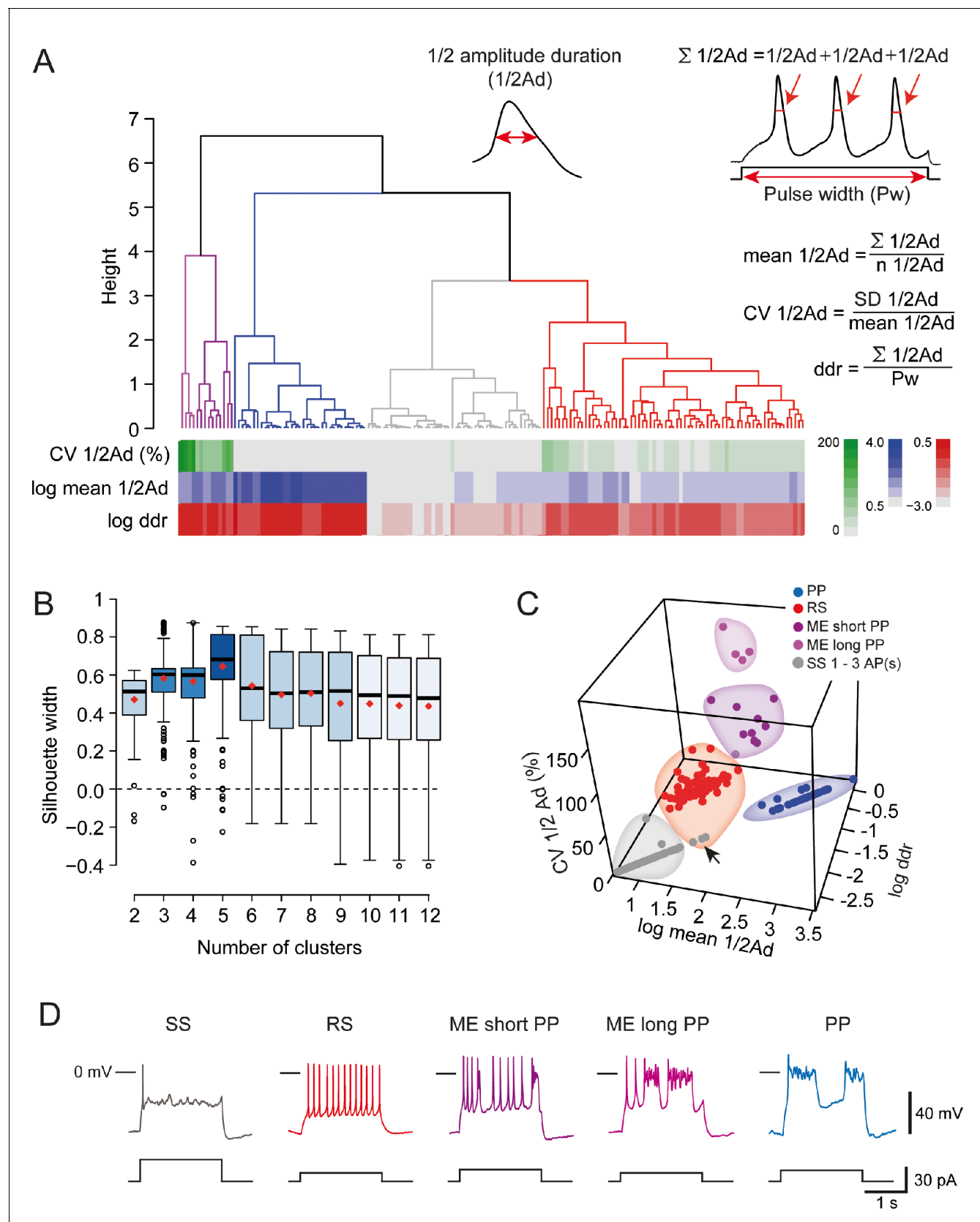


Figure 3. Cluster analysis of V1^R firing pattern at E12.5. (A, insets) Cluster analysis of embryonic V1^R firing pattern was performed using three parameters that describe the firing pattern during a 2 s suprathreshold depolarizing pulses: the mean of the half-amplitude event duration (mean 1/2Ad), Figure 3 continued on next page

Figure 3 continued

the coefficient of variation of $\frac{1}{2}Ad$ ($CV \frac{1}{2}Ad$) allowing to quantify the action potential variation within a train (CV was set to 0 when the number of spikes evoked by a depolarizing pulse was ≤ 3) and the duration ratio $ddr = \Sigma \frac{1}{2}Ad/Pw$, obtained by dividing the sum of $\frac{1}{2}Ad$ by the pulse duration Pw , that indicates the total time spent in the depolarized state. For example, $ddr = 1$ when a plateau potential (PP) lasts as long as the depolarizing pulse. Conversely, its value is low when the depolarizing pulse evokes a single AP only. (A) Dendrogram for complete linkage hierarchical clustering of 164 embryonic $V1^R$ ($N = 140$) according to the values of log mean $\frac{1}{2}Ad$, $CV \frac{1}{2}Ad$, and log ddr . The colored matrix below the dendrogram shows the variations of these three parameters for all the cells in the clusters (colored trees) extracted from the dendrogram. (B) The number of clusters was determined by analyzing the distribution of silhouette width values (see Materials and methods). The box plots show the distribution of silhouette width values when the number of clusters k varies from 2 to 12. The mean silhouette width values (red diamond-shaped points) attained their maximum when the estimated cluster number was 5. (C) 3D plot showing cluster distribution of embryonic $V1^R$ according to log mean $\frac{1}{2}Ad$, $CV \frac{1}{2}Ad$, and log ddr . Each cluster corresponds to a particular firing pattern as illustrated in (D). $V1^R$ that cannot sustain repetitive firing of APs (1–3 AP/pulse only, gray, single spiking [SS]), $V1^R$ that can fire tonically (red, repetitive spiking [RS]), $V1^R$ with a firing pattern characterized by a mix of APs and relatively short PPs (dark purple, mixed event short PP [ME short PP]), $V1^R$ with a firing pattern characterized by a mix of APs and relatively long plateau potentials (light purple, mixed event long PP [ME long PP]), and $V1^R$ with evoked PPs only (blue, PP). The arrow in (C) indicates three misclassified $V1^R$ that could not sustain repetitive firing although they were assigned to the cluster of repetitively firing $V1^R$ (see text).

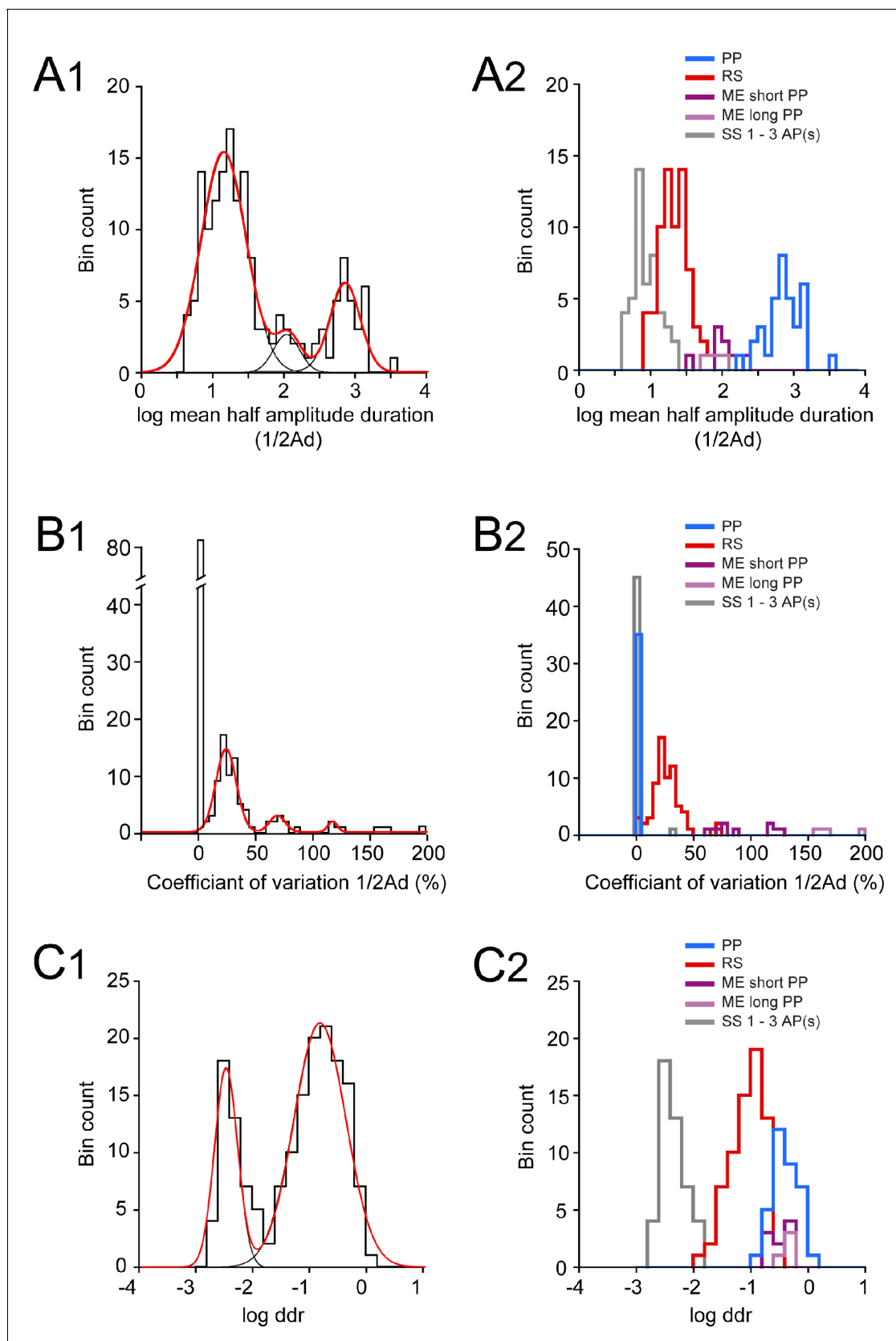


Figure 3—figure supplement 1. Distributions of log half-amplitude event duration ($\log 1/2Ad$), coefficient of variation of $1/2Ad$ ($CV 1/2Ad$), and log depolarizing duration ratio ($\log ddr$) values related to the cluster analysis of embryonic $V1^R$ firing patterns. (A1) Histogram of log mean $1/2Ad$ for the Figure 3—figure supplement 1 continued on next page

Figure 3—figure supplement 1 continued

whole $V1^R$ population at E12.5 ($n = 164$; bin width 0.1). The histogram was well fitted by the sum of three Gaussian curves with means and SDs of 1.135, 2.046, and 2.84, and 0.316, 0.181, and 0.21, respectively. **(A2)** Histogram of the values of log mean $\frac{1}{2}Ad$ sorted after cluster analysis showing single spiking (SS) $V1^R$ (gray), repetitive spiking (RS) $V1^R$ (red), mixed events (ME) $V1^R$ with short plateau potentials (ME short PP $V1^R$, light purple), ME $V1^R$ with long plateau potentials (ME long PP $V1^R$, dark purple), and PP $V1^R$ (blue). log mean $\frac{1}{2}Ad$ was significantly different between SS $V1^R$, PP $V1^R$, the whole ME $V1^R$ population (ME_s and ME_l $V1^R$), and PP $V1^R$ (Kruskal–Wallis test $p < 0.0001$; SS $V1^R$ versus RS $V1^R$, $p < 0.0001$; SS $V1^R$ versus ME $V1^R$, $p < 0.0001$; SS $V1^R$ versus PP $V1^R$, $p < 0.0001$; RS $V1^R$ versus ME $V1^R$, $p = 0.0004$; RS $V1^R$ versus PP $V1^R$, $p < 0.0001$; ME $V1^R$ versus PP $V1^R$, $p = 0.018$; SS $V1^R$ $n = 46$, RS $V1^R$ $n = 69$, ME_s $V1^R$ $n = 9$, ME_l $V1^R$ $n = 4$, PP $V1^R$ $n = 35$). **(B1)** Histogram of CV $\frac{1}{2}Ad$ for the whole $V1^R$ population at E12.5 ($n = 164$; bin width 5%). Note that a large population of $V1^R$ had zero CV $\frac{1}{2}Ad$ ($n = 83$). The histogram for CV $\frac{1}{2}Ad \neq 0$ was fitted by the sum of three Gaussian curves with means and SDs of 23.4, 68.4, and 117 (%) and 8.9, 6.8, and 4.1, respectively. **(B2)** Histograms of the values of CV $\frac{1}{2}Ad$ sorted after cluster analysis showing SS $V1^R$ (black), RS $V1^R$ (red), ME_s $V1^R$ (light purple), ME_l $V1^R$ (dark purple), and PP $V1^R$. CV $\frac{1}{2}Ad$ was not significantly different between SS $V1^R$ and PP $V1^R$ (CV $\frac{1}{2}Ad$ of SS $V1^R$ and PP $V1^R$ = 0.682% and 0%, respectively: only one of the 46 SS $V1^R$ displayed 3 PA and had a CV $\frac{1}{2}Ad$ of 31.37). CV $\frac{1}{2}Ad$ was significantly different between RS $V1^R$ and the whole ME $V1^R$ population and also between SS $V1^R$ or PP $V1^R$ and RS $V1^R$ or ME $V1^R$ (Kruskal–Wallis test $p < 0.0001$; SS $V1^R$ versus RS $V1^R$, $p < 0.0001$; SS $V1^R$ versus ME $V1^R$, $p < 0.0001$; SS $V1^R$ versus PP $V1^R$, $p = 0.846$; RS $V1^R$ versus ME $V1^R$, $p = 0.0003$; RS $V1^R$ versus PP $V1^R$, $p < 0.0001$; ME $V1^R$ versus PP $V1^R$, $p < 0.0001$). **(C1)** Histogram of log ddr (sum of $\frac{1}{2}Ad$ divided by pulse duration) for the whole $V1^R$ population at E12.5 ($n = 164$; bin width 0.2). The histogram was fitted by the sum of two Gaussian curves with means and SDs of -2.51 and -0.851 , and 0.2 and 0.46, respectively. **(C2)** Histograms of the values of log ddr sorted after cluster analysis showing SS $V1^R$ (black), RS $V1^R$ (red), ME_s $V1^R$ (light purple), ME_l $V1^R$ (dark purple), and PP $V1^R$. log (ddr) was not significantly different between ME $V1^R$ and PP $V1^R$, while it was significantly different between SS $V1^R$ and RS $V1^R$, SS $V1^R$ and the whole ME $V1^R$ population, SS $V1^R$ and PP $V1^R$, RS $V1^R$ and the whole ME $V1^R$ population, RS $V1^R$ and PP $V1^R$ (Kruskal–Wallis test $p < 0.0001$; SS $V1^R$ versus RS $V1^R$, $p < 0.0001$; SS $V1^R$ versus ME $V1^R$, $p < 0.0001$; SS $V1^R$ versus PP $V1^R$, $p < 0.0001$; RS $V1^R$ versus ME $V1^R$, $p < 0.0001$; RS $V1^R$ versus PP $V1^R$, $p < 0.0001$; ME $V1^R$ versus PP $V1^R$, $p = 0.977$). ME_s $V1^R$ and ME_l $V1^R$ differed only by their CV $\frac{1}{2}Ad$ (Mann–Whitney test, log mean $\frac{1}{2}Ad$ for ME_s $V1^R$ versus log mean $\frac{1}{2}Ad$ for ME_l $V1^R$, $p = 0.26$; CV $\frac{1}{2}Ad$ for ME_s $V1^R$ versus CV $\frac{1}{2}Ad$ ME_l $V1^R$, $p = 0.0028$ and log ddr for ME_s $V1^R$ versus log ddr for ME_l $V1^R$, $p = 0.1483$). It is noteworthy that the distribution of the values of each metric was multimodal, thus indicating that each of them could partially discriminate different groups of embryonic $V1^R$ according to their firing pattern.

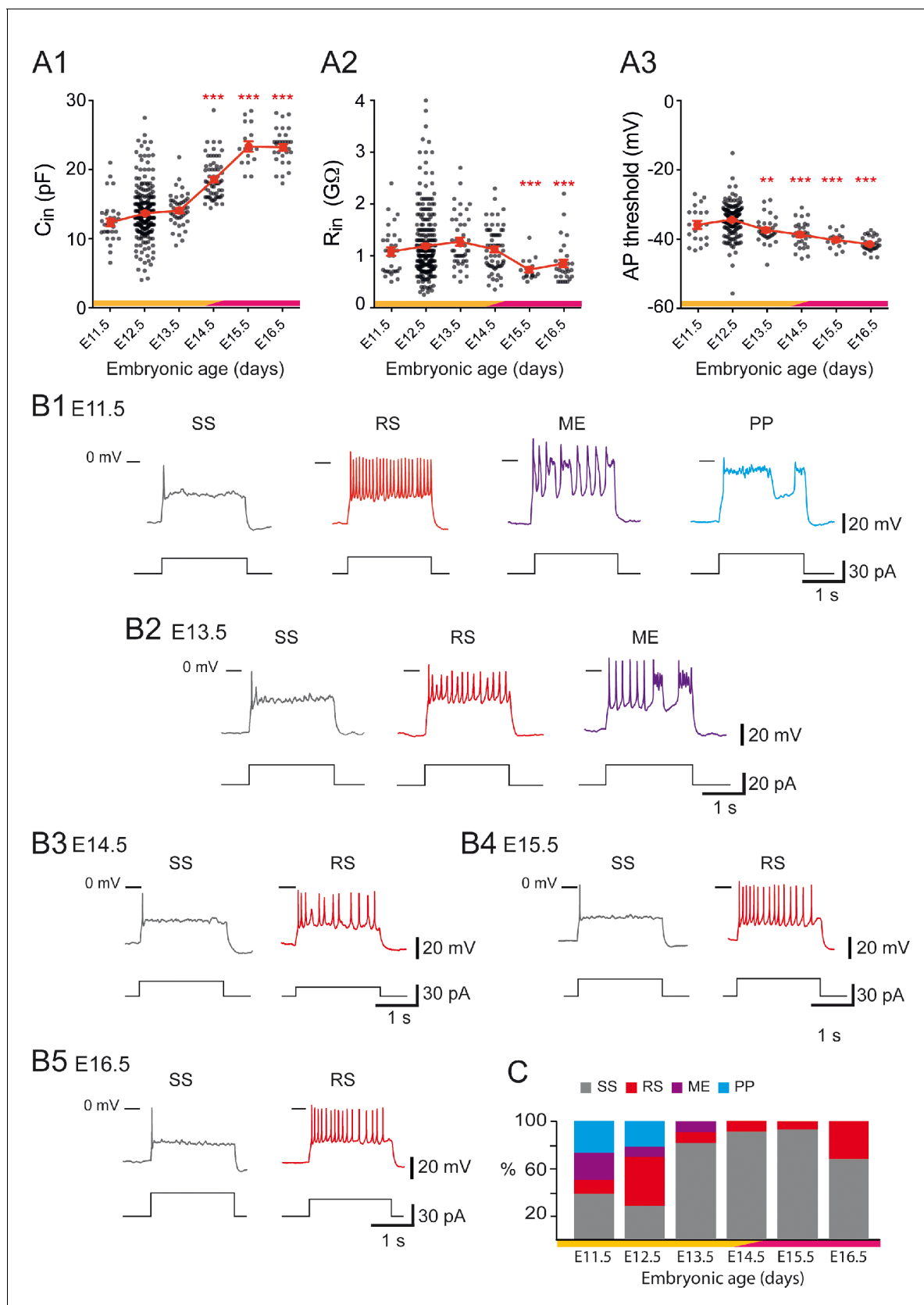


Figure 4. Developmental changes of embryonic $V1^R$ firing patterns from E11.5 to E16.5. (A1) Graph showing how the input capacitance C_{in} of $V1^R$ changes with embryonic age. C_{in} significantly increased between E12.5 or E13.5 and E14.5 (Kruskal-Wallis test $p < 0.0001$; E12.5 versus E11.5 $p = 0.258$, Figure 4 continued on next page

Figure 4 continued

E12.5 versus E13.5 $p=0.904$, E12.5 versus E14.5 $p<0.0001$, E12.5 versus E15.5 $p<0.0001$, E12.5 versus E16.5 $p<0.0001$, E13.5 versus E14.5 $p<0.0001$, E13.5 versus E15.5 $p<0.0001$, E13.5 versus E16.5 $p<0.0001$; E11.5 $n = 31$; $N = 27$, E12.5 $n = 267$; $N = 152$, E13.5 $n = 43$; $N = 40$, E14.5 $n = 61$; $N = 49$, E15.5 $n = 16$; $N = 4$, E16.5 $n = 30$; $N = 9$). (A2) Graph showing how the input resistance R_{in} of $V1^R$ changes with embryonic age. R_{in} significantly decreased between E12.5 or E14.5 and E15.5 (Kruskal–Wallis test $p<0.0001$; E12.5 versus E11.5 $p>0.999$, E12.5 versus E13.5 $p=0.724$, E12.5 versus E14.5 $p>0.999$, E12.5 versus E15.5 $p=0.0004$, E12.5 versus E16.5 $p=0.0005$, E14.5 versus E15.5 $p=0.0019$, E14.5 versus E16.5 $p<0.0058$; E11.5 $n = 31$, E12.5 $n = 261$; $N = 146$, E13.5 $n = 43$; $N = 40$, E14.5 $n = 60$; $N = 48$, E15.5 $n = 16$; $N = 4$, E16.5 $n = 30$; $N = 9$). (A3) Graph showing how the threshold of regenerative events (action potentials [APs] and plateau potentials [PP]) of $V1^R$ changes with embryonic age. The average threshold became significantly more hyperpolarized after E12.5 (Kruskal–Wallis test $p<0.0001$; E12.5 versus E11.5 $p=0.676$, E12.5 versus E13.5 $p=0.0039$, E12.5 versus E14.5 $p<0.0001$, E12.5 versus E15.5 $p<0.0001$, E12.5 versus E16.5 $p<0.0001$, E13.5 versus E14.5 $p>0.999$, E13.5 versus E15.5 $p=0.1398$, E13.5 versus E16.5 $p=0.0013$; E14.5 versus E15.5 $p>0.999$, E14.5 versus E16.5 $p=0.0634$, E15.5 versus E16.5 $p>0.999$; E11.5 $n = 20$; $N = 16$, E12.5 $n = 162$; $N = 139$, E13.5 $n = 31$; $N = 28$, E14.5 $n = 30$; $N = 26$, E15.5 $n = 16$; $N = 4$, E16.5 $n = 30$; $N = 9$). Yellow and purple bars below the graphs indicate the two important phases of the functional development of spinal cord networks. The first one is characterized by synchronized neuronal activity (SNA), and the second one is characterized by the emergence of a locomotor-like activity (see text). Note that changes in C_{in} and R_{in} occurred at the end of the first developmental phase (* $p<0.05$, ** $p<0.01$, *** $p<0.001$; control, E12.5). The intrinsic activation properties were analyzed using 2 s suprathreshold depolarizing current steps. (B) Representative traces of voltage responses showing single spiking (SS) $V1^R$ (gray), repetitive spiking (RS) $V1^R$ (red), mixed events (ME) $V1^R$ (purple), and PP $V1^R$ (blue) at E11.5 (B1), E13.5 (B2), E14.5 (B3), E15.5 (B4), and E16.5 (B5). (C) Bar graph showing how the proportions of the different firing patterns change from E11.5 to E16.5 (E11.5 $n = 22$; $N = 18$, E12.5 $n = 163$; $N = 140$, E13.5 $n = 32$; $N = 29$, E14.5 $n = 57$; $N = 45$, E15.5 $n = 15$; $N = 4$, E16.5 $n = 28$; $N = 9$). Yellow and purple bars below the graphs indicate the first and the second phase of functional embryonic spinal cord networks. The proportions of the different firing patterns significantly changed between E11.5 to E12.5 (Fisher's exact test, $p=0.0052$) with a significant increase in the proportion of RS $V1^R$ (Fisher's exact test, $p=0.0336$) and a significant decrease in the proportion of ME $V1^R$ (Fisher's exact test, $p=0.01071$) at E12.5. Only two firing patterns (SS and RS) were observed after E13.5 and most embryonic $V1^R$ lost their ability to sustain tonic firing after E13.5. However, at E16.5 the proportion of RS $V1^R$ significantly increased at the expense of SS $V1^R$ when compared to E14.5 (Fisher's exact test, $p=0.0112$), indicating that embryonic $V1^R$ began to recover the ability to sustain tonic firing after E15.5.

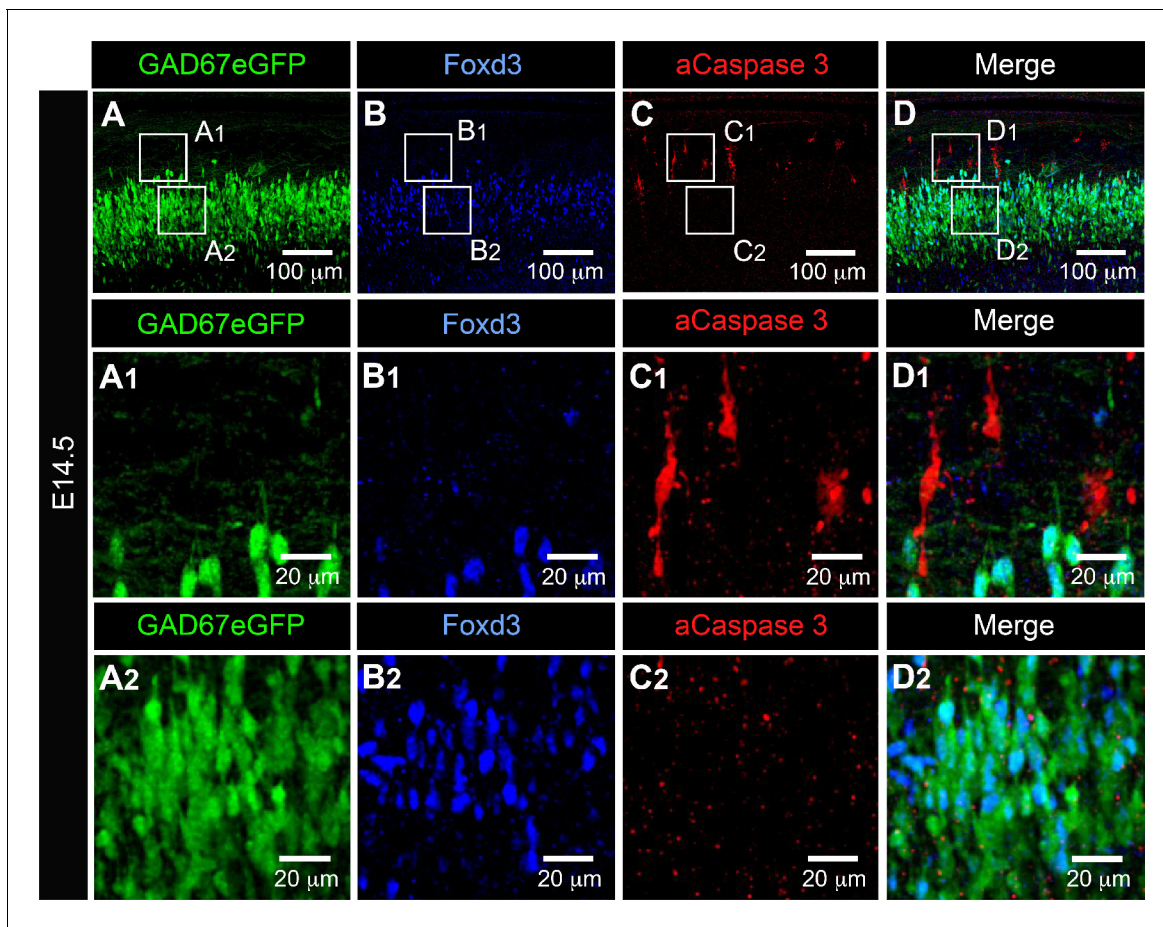


Figure 5. Activated caspase3 (aCaspase3) is not observed in embryonic V1^R at E14.5. Representative confocal image of the ventral part of an isolated lumbar spinal cord of E14.5 GAD67-eGFP mouse embryo showing immunostainings using antibodies against eGFP (A), FoxD3 (B), and aCaspase3 (C). (D) Superimposition of the three stainings shows that embryonic V1^R (eGFP+ and FoxD3+) were not aCaspase three immunoreactive. (A1, B1, C1, and D1). Enlarged images from (A), (B), and (C) showing that aCaspase3 staining is localized in areas where eGFP and Foxd3 staining were absent. (A2, B2, C2, and D2) Enlarged images from (A), (B), and (C) showing that aCaspase3 staining is absent in the area where V1^R (eGFP+ and FoxD3+) are located. aCaspase3 staining that did not co-localize with GAD67eGFP likely indicates motoneuron developmental cell death.

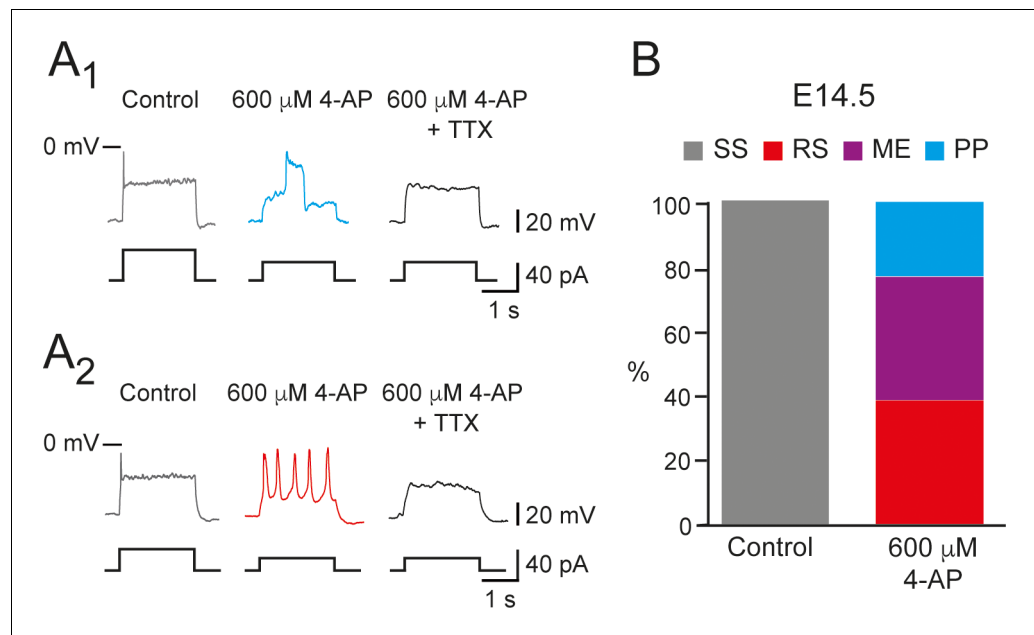


Figure 6. 600 μM 4-aminopyridine (4-AP) changed the firing pattern of single spiking (SS) embryonic V1^R recorded at E14.5. The firing pattern of embryonic V1^R was evoked by 2 s suprathreshold depolarizing current steps. (A) Representative traces showing the effect of 4-AP application (600 μM) on the firing pattern of SS V1^R recorded at E14.5. Note that the applications of 600 μM 4-AP evoked either a plateau potential (PP, A₁) or repetitive spiking (RS, A₂), both fully blocked by tetrodotoxin. (B) Bar plots showing the proportions of the different firing patterns observed in the presence of 600 μM 4-AP versus control recorded in SS V1^R at E14.5 (n = 14; N = 14). SS V1^R (gray), RS V1^R (red), mixed Events (ME) V1^R (purple), and PP V1^R (blue).

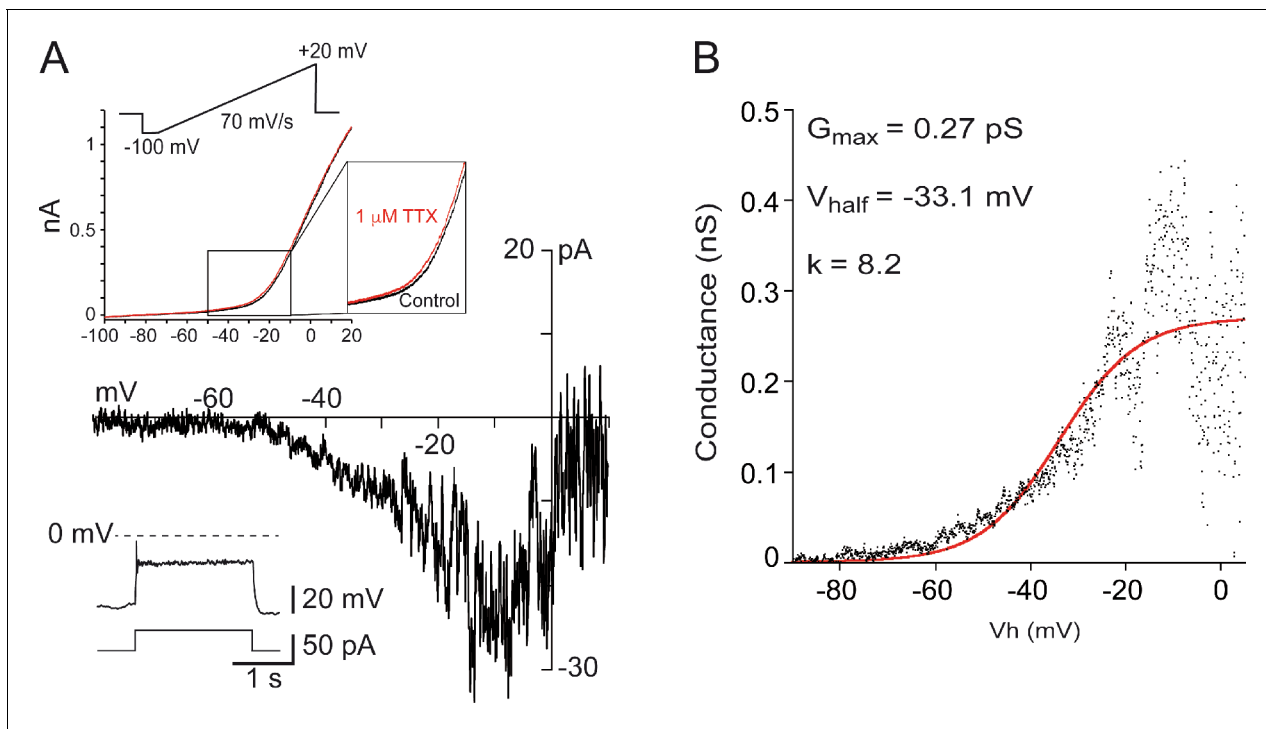


Figure 6—figure supplement 1. I_{Nap} is present in embryonic $V1^R$ recorded at E14.5. (A) Representative trace of I_{Nap} evoked by a slow depolarizing voltage ramp (70 mV/s, upper inset) in single spiking (SS) embryonic $V1^R$ (lower inset). I_{Nap} was isolated by subtracting currents evoked by depolarizing ramps in the presence of 1 μ M tetrodotoxin (TTX) to the control current evoked in the absence of TTX (upper inset). (B) Voltage dependence of G_{Nap} conductance calculated from the trace shown in (A). The activation curve was obtained by transforming the current evoked by a depolarizing voltage ramp from -100 mV to 20 mV (70 mV/s) using the following equation: $G_{Nap} = -I_{Nap}/((-V_h) + E_{Na})$, where V_h is the holding potential at time t during a depolarizing voltage ramp and E_{Na} is the equilibrium potential for sodium ($E_{Na} = 60$ mV). The G_{Nap}/V_h curve was fitted with the following Boltzmann function: $G = G_{MAX}/(1 + \exp(-(V - V_{HALF})/k))$ (Boeri et al., 2018), where V_{half} is the V_h value for G_{Nap} half activation, k the slope factor of the curve, and G_{max} the maximum conductance. We found no significant difference between the values of V_{half} (Mann-Whitney test: $p=0.8518$) and of k (Mann-Whitney test: $p=0.7546$) obtained at E12.5 (Boeri et al., 2018) and those obtained at E14.5. At E14.5, $V_{half} = -27 \pm 5.1$ mV and $k = 7.73 \pm 0.78$ ($n = 6$).

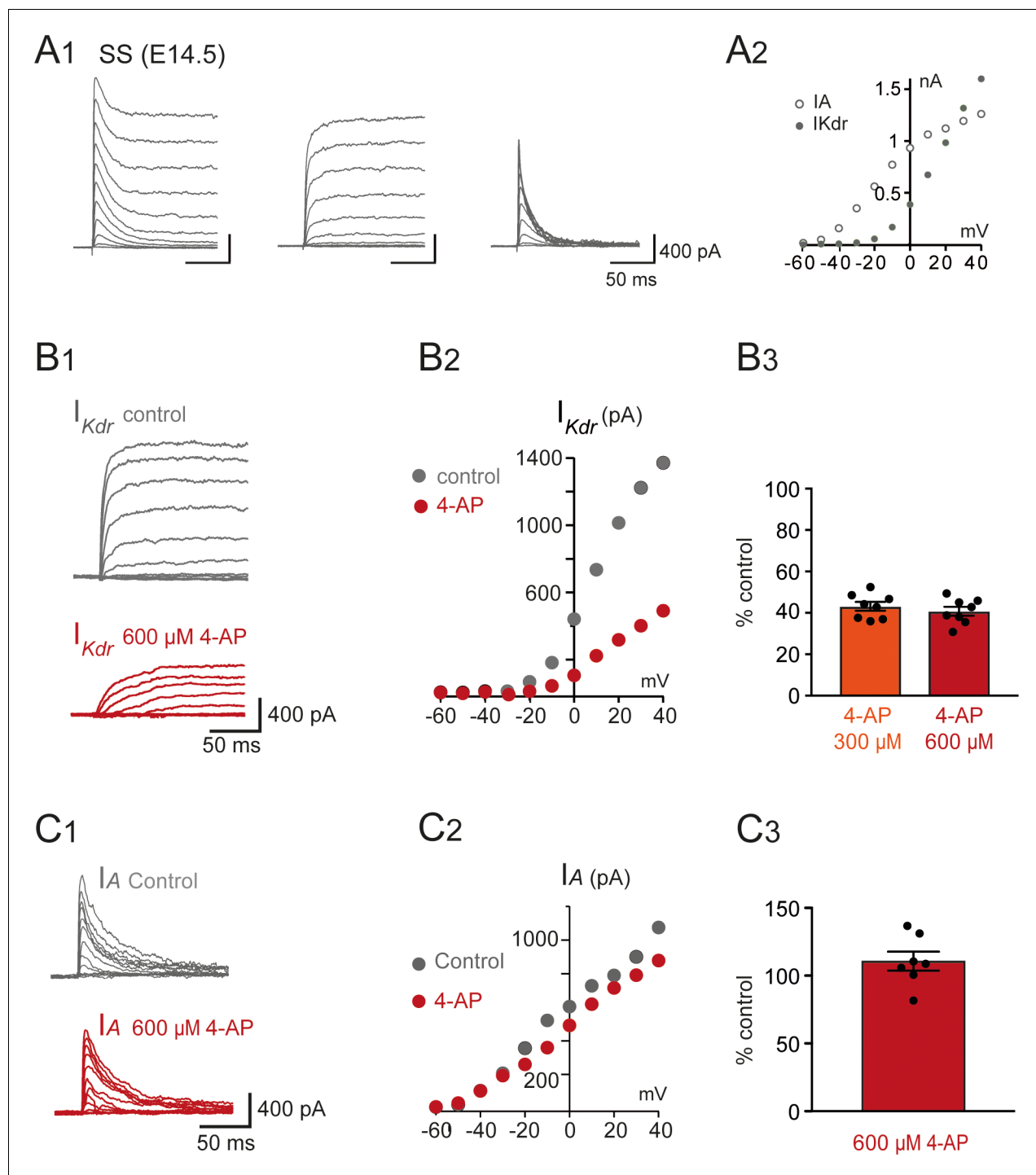


Figure 6—figure supplement 2. I_{Kdr} was inhibited by 4-aminopyridine (4-AP) in $V1^R$ recorded at E14.5. (A1) Representative examples of the total outward K^+ currents obtained from $V_H = -100$ mV (left traces), I_{Kdr} ($V_H = -30$ mV, middle traces), and isolated I_A (left traces) recorded in single spiking (SS) $V1^R$ at E14.5. (A2) Current-voltage relationship of I_{Kdr} (filled circle) and I_A (open circle) in SS $V1^R$ at E14.5. $I-V$ curves were obtained from currents shown in (A1). (B1) Representative example of the effect of 4-AP at 600 μ M in $V1^R$ at E14.5. (B2) Current-voltage curves in control condition and in the presence of 600 μ M 4-AP. (B3) Bar plots showing the percentage of I_{Kdr} inhibition evoked by 300 μ M 4-AP application ($n = 8$) and 600 μ M 4-AP application ($n = 7$). The percentages of I_{Kdr} inhibition evoked by 300 μ M 4-AP and 600 μ M 4-AP applications were not significantly different ($p=0.574$). (C1) Representative example of the effect of 600 μ M 4-AP on I_A in $V1^R$ recorded at E14.5. (C2) $I-V$ curves in control conditions and in the presence of 600 μ M 4-AP. These curves were obtained from the traces shown in (B1). (C3) Bar graph showing the percentage of I_A block elicited by 4-AP. 4-AP did not significantly block I_A (Wilcoxon test $p=0.11$, $n = 6$).

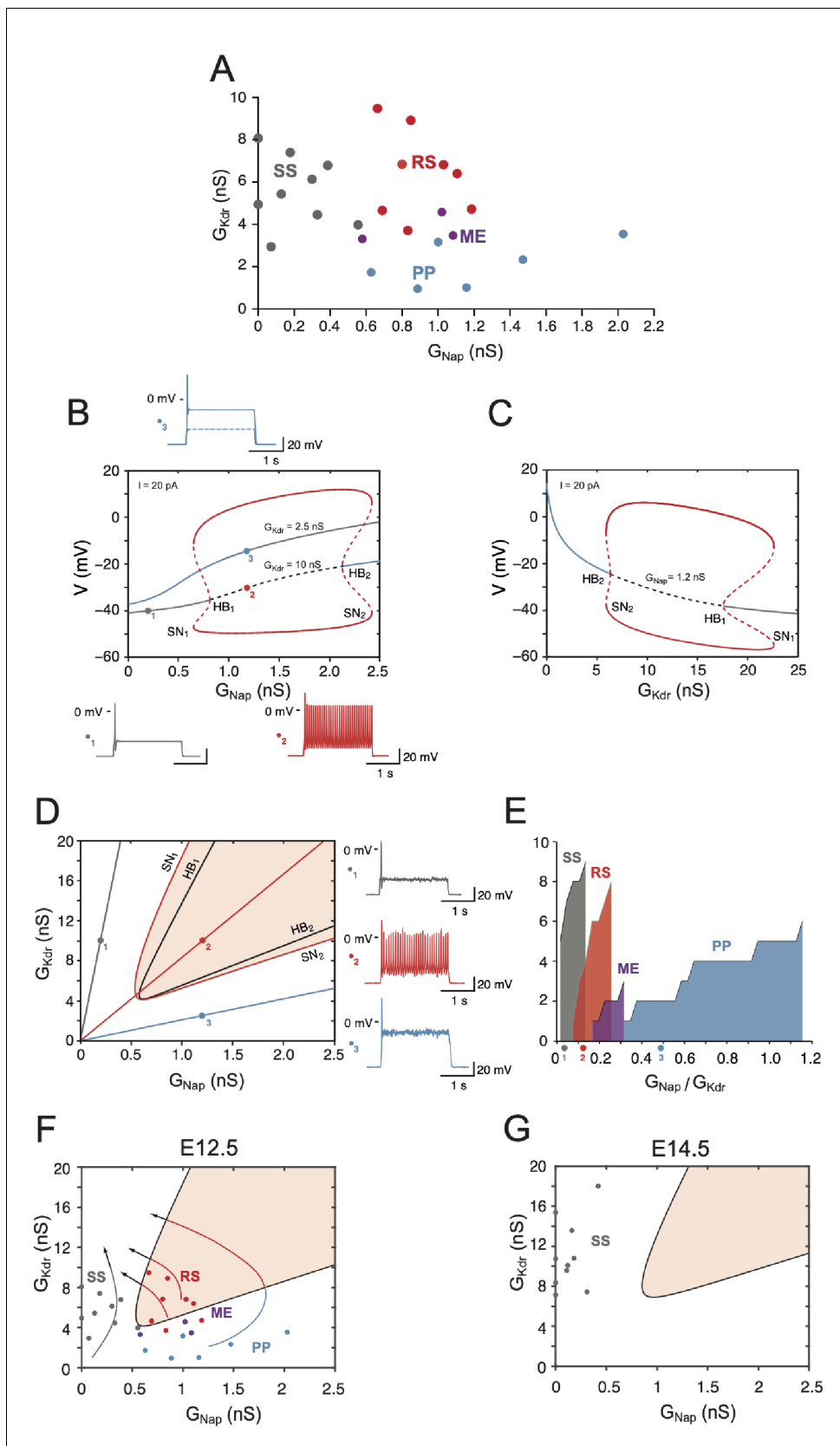


Figure 7. Embryonic V1^R firing patterns predicted by computational modeling. (A) Firing patterns of 26 recorded cells, in which both G_{Nap} and G_{Kdr} were measured. Gray: single spiking (SS); red: repetitive spiking (RS); blue: plateau potential (PP). The three purple points located at the boundary

Figure 7 continued on next page

Figure 7 continued

between the RS and PP regions correspond to mixed events (ME), where plateau potentials alternate with spiking episodes. Note that no cell exhibited low values of both G_{Nap} and G_{Kdr} (lower left) or large values of both conductances (upper right). **(B)** Bifurcation diagram of the deterministic model when G_{Kdr} is kept fixed to 2.5 nS or 10 nS while G_{Nap} is varied between 0 and 2.5 nS. $G_{in} = 1$ nS and $I = 20$ pA. For $G_{Kdr} = 10$ nS (i.e., in the top experimental range), the red curves indicate the maximal and minimal voltages achieved on the stable limit cycle associated with repetitive firing (solid lines) and on the unstable limit cycle (dashed lines). The fixed point of the model is indicated by a gray solid line when it corresponds to a stable quiescent state, a gray dashed line when it is unstable, and a solid blue line when it corresponds to a stable plateau potential. The two Hopf bifurcations (HB) corresponding to the change of stability of the quiescence state (HB₁, $G_{Nap} = 0.81$ nS) and the voltage plateau (HB₂, $G_{Nap} = 2.13$ nS) are indicated, as well as the two saddle node (SN) bifurcations of limit cycles associated with the onset (SN₁, $G_{Nap} = 0.65$ nS) and offset (SN₂, $G_{Nap} = 2.42$ nS) of repetitive spiking as G_{Nap} is increased. For $G_{Kdr} = 2.5$ nS, the model does not display repetitive firing; it possesses a unique fixed point, which is always stable (blue-gray curve). The transition from quiescence to plateau is gradual with no intervening bifurcation. Representative voltage traces of the three different activity patterns are shown: SS in response to a 2 s current pulse (gray, $G_{Nap} = 0.2$ nS, $G_{Kdr} = 10$ nS), RS (red, $G_{Nap} = 1.2$ nS, $G_{Kdr} = 10$ nS), and PP (blue, $G_{Nap} = 1.2$ nS, $G_{Kdr} = 2.5$ nS). Note that the plateau never outlasts the current pulse. **(C)** Bifurcation diagram when G_{Nap} is kept fixed at 1.2 nS and G_{Kdr} is varied between 0 and 25 nS ($I = 20$ pA). Same conventions as in **(B)**. PP is stable until the subcritical HB₂ ($G_{Kdr} = 6.34$ nS) is reached, repetitive firing can be observed between SN₂ ($G_{Kdr} = 5.93$ nS) and SN₁ ($G_{Kdr} = 22.65$ nS). The quiescent state is stable from point HB₁ ($G_{Kdr} = 17.59$ nS) onward. **(D)** Two-parameter bifurcation diagram of the model in the G_{Nap} - G_{Kdr} plane ($I = 20$ pA). The black curves indicate the bifurcations HB₁ and HB₂. The red curves indicate the SN bifurcations of limit cycles SN₁ and SN₂. The shaded area indicates the region where repetitive firing can occur. The oblique lines through the points labeled 1, 2, and 3, the same as in **(B)**, correspond to three different values of the ratio of G_{Nap} / G_{Kdr} : 0.02 (gray), 0.12 (red), and 0.48 (blue). Voltage traces on the right display the response to a 2 s current pulse when channel noise is taken into account for the three regimes: SS (top, gray trace and dot in the diagram), RS (middle, red), and PP (bottom, blue). They correspond to the three deterministic voltage traces shown in **(B)**. Note that the one-parameter bifurcation diagrams shown in **(B)** correspond to horizontal lines through points 1 and 2 ($G_{Kdr} = 10$ nS) and through point 3 ($G_{Kdr} = 2.5$ nS), respectively. The bifurcation diagram in **(C)** corresponds to a vertical line through points 2 and 3 ($G_{Nap} = 1.2$ nS). **(E)** Cumulative distribution function of the ratio G_{Nap} / G_{Kdr} for the four clusters in **(A)**, showing the sequencing SS (gray) → RS (red) → ME (purple, three cells only) → PP (blue) predicted by the two-parameter bifurcation diagram in **(D)**. The wide PP range, as compared to SS and RS, merely comes from the fact that G_{Nap} is small for cells in this cluster. The three colored points indicate the slopes of the oblique lines displayed in **(D)**. **(F)** The data points in **(A)** are superimposed on the two-parameter bifurcation diagram shown in **(D)**, demonstrating a good agreement between our basic model and experimental data (same color code as in **A** for the different clusters). The bifurcation diagram is simplified compared to **(A)**, only the region where repetitive spiking is possible (i.e., between the lines SN₁ and SN₂ in **A**) being displayed (shaded area). Notice that three ME cells (purple dots) are located close to the transition between the RS and PP regions. The four arrows indicate the presumable evolution of G_{Nap} and G_{Kdr} for SS, RS, ME, and PP cells between E12.5 and E14.5–15.5. G_{Nap} eventually decreases while G_{Kdr} keeps on increasing. **(G)** Distribution of a sample of cells in the G_{Nap} - G_{Kdr} plane at E14.5. All the cells are located well within the SS region far from bifurcation lines because of the decreased G_{Nap} compared to E12.5, the increased G_{Kdr} , and the shift of the RS region (shaded) due to capacitance increase (18 versus 13 pF).

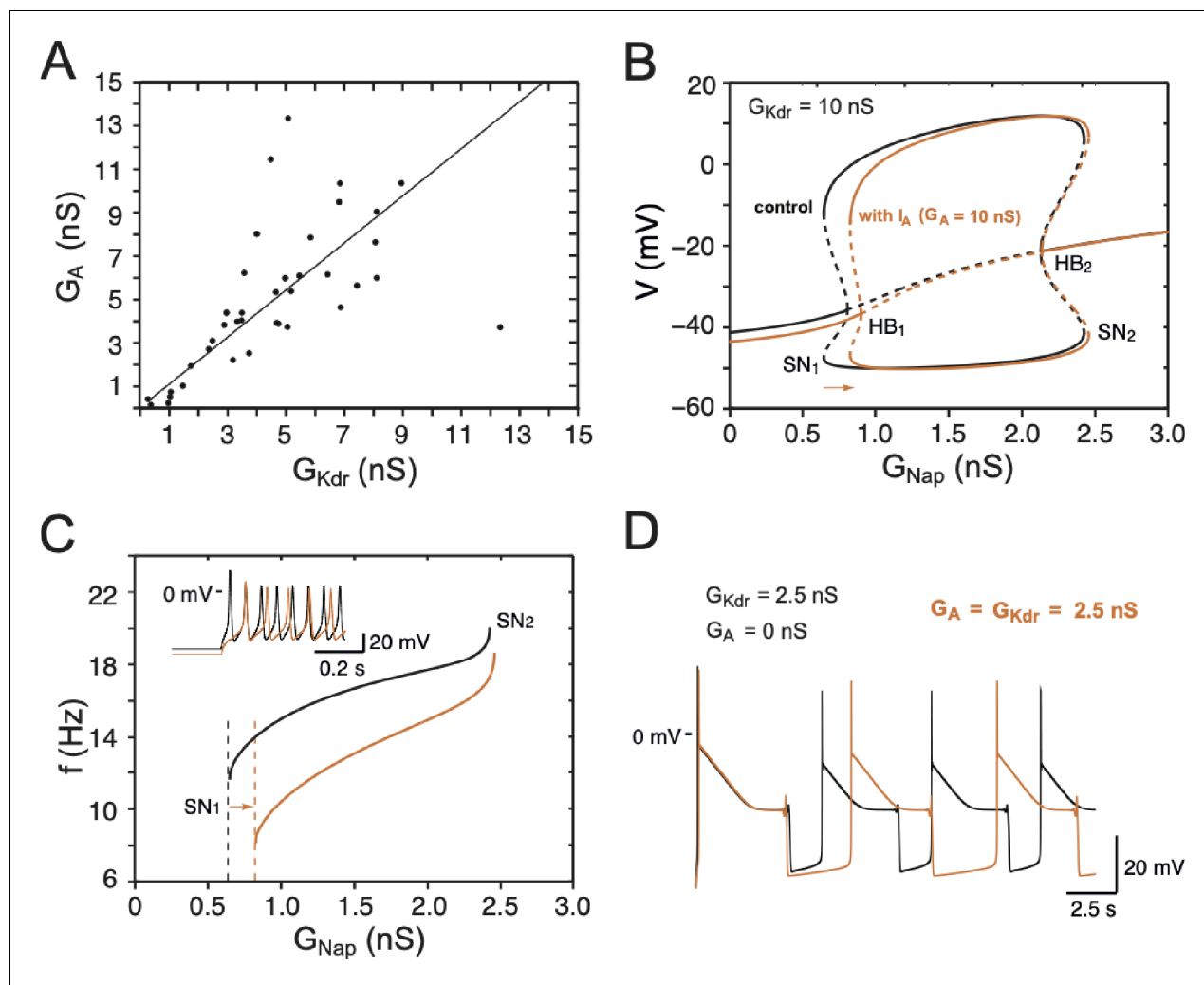


Figure 7—figure supplement 1. Effect of I_A on embryonic $V1^R$ firing patterns predicted by computational modeling. (A) The maximal conductances of I_{Kdr} and I_A at E12.5 are linearly correlated. Best fit: $G_A = 1.09 G_{Kdr}$ ($R^2 = 0.81$, $N = 44$). (B) Effect of I_A on the dynamics of the basic model. The one-parameter bifurcation diagrams in control condition (black, $I = 20$ pA, $G_{Kdr} = 10$ nS, no I_A same as in **Figure 7B**) and with I_A added (orange, $G_A = 10$ nS) are superimposed. The I_A current shifts the firing threshold SN_1 to the right by 0.18 nS (see also C) as indicated by the orange arrow, with little effect on the amplitude of action potentials (see also inset in C). In contrast, I_A shifts SN_2 by only 0.03 nS because it is inactivated by depolarization. (C) I_A also slows down the discharge frequency, as shown by comparing the $G_{Nap} - V$ curves without I_A (black) and with I_A (orange). For $G_{Nap} = 1$ nS, for instance, the firing frequency is reduced by 31%, from 15 to 10.4 Hz. Here again, the effect of I_A progressively decreases as G_{Nap} increases because of the membrane depolarization elicited by I_{Nap} . For $G_{Nap} = 2.4$ nS, for instance, the firing frequency is reduced by 11% only, from 19.1 to 17 Hz. This frequency reduction elicited by I_A does not merely result from the increased firing threshold. Note also that the latency of the first spike is increased (see voltage trace in inset), which is a classical effect of I_A . (D) I_A reduces the frequency of pseudo-plateau bursting by lengthening quiescent episodes (doubling their duration in the example shown) without affecting the duration of plateaus much (here a mere 5% increase), as shown by the comparison of the voltage traces obtained without I_A (control, $G_{Kdr} = 2.5$ nS, black) and with I_A ($G_{Kdr} = G_A = 2.5$ nS, orange). This is because I_A is activated near rest but inactivated during voltage plateaus. Note that increasing G_{Kdr} in the absence of I_A has not the same effect; it shortens both plateaus and quiescent episodes (see **Figure 8C**, where $G_{Kdr} = 5$ nS). This is because I_{Kdr} does not inactivate (or does it only very slowly) in contrast to I_A .

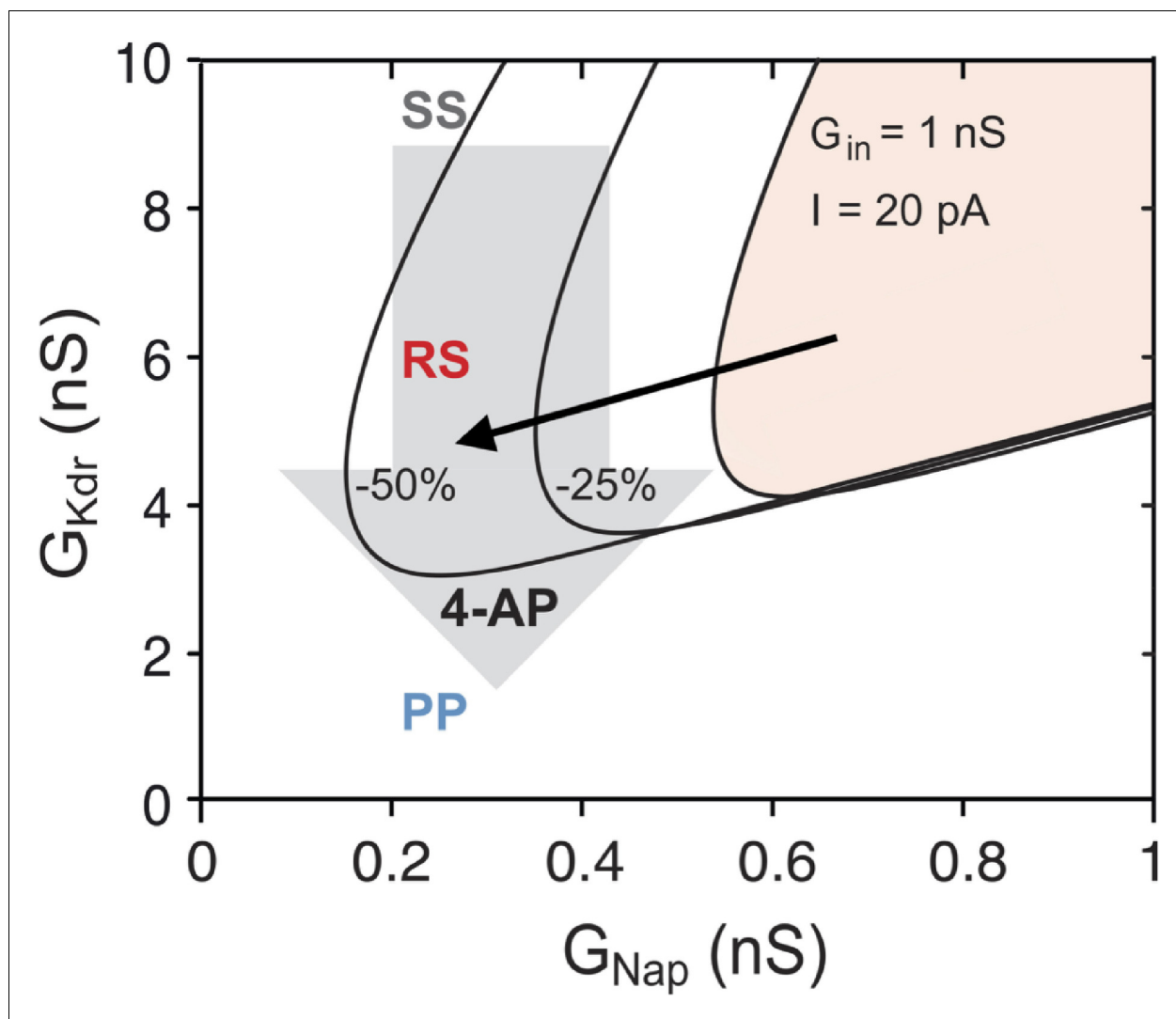


Figure 7—figure supplement 2. Explaining the effect of 4-aminopyridine (4-AP) on the firing pattern. The R region of the basic model, where repetitive firing may occur, is displayed in the $G_{\text{Nap}} - G_{\text{Kdr}}$ plane in control condition for E12.5 V1^R ($C_{\text{in}} = 13$ pF, $G_{\text{in}} = 1$ nS, $I = 20$ pA, shaded area) and when G_{in} and I were both reduced by 25% (middle curve) or 50% (left curve). The reduced I accounts for the decrease in rheobase, and thus in the current injected in the experiments, following the decrease in G_{in} . If 4-AP reduced only G_{Kdr} (as indicated by the downward arrow), the firing pattern of SS V1^R would not change, the RS region being too far to the right to be visited. In contrast, when the effects of 4-AP on the input conductance and rheobase are taken into account, the bifurcation diagram moves leftward and downward, as indicated by the oblique black arrow, and the RS and PP regions are then successively entered as G_{Kdr} is reduced. The same explanation holds at E14.5.

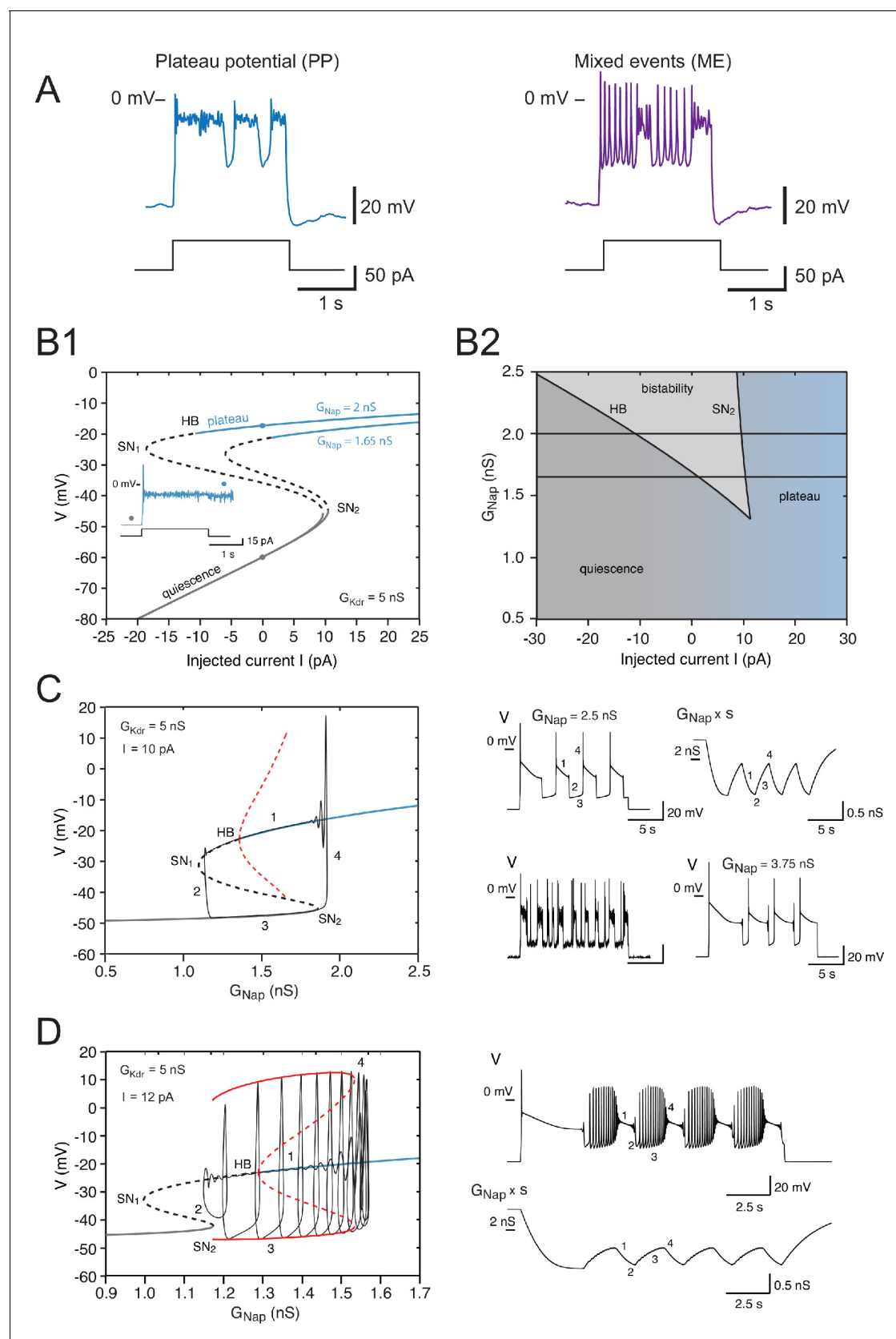


Figure 8. Effects of the slow inactivation of I_{Nap} on firing patterns predicted by computational modeling. **(A)** Examples of repetitive plateaus (left) and mixed events (right) recorded in V1^R at E12.5 during a 2 s current pulse. **(B1)** Current-voltage curve of the basic model (without slow inactivation of I_{Nap} and without I_A or channel noise) for $G_{Kdr} = 5$ nS and for $G_{Nap} = 1.65$ nS (lower curve) and 2 nS (upper curve). Solid lines denote stable fixed points and dashed lines unstable ones. For $G_{Nap} = 1.65$ nS, bistability between quiescence and plateau occurs between 1.39 and 10.48 pA. When G_{Nap} is increased to 2 nS, the bistability region ranges from -10.84 to 9.70 pA, thus extending into the negative current range. This implies that once a plateau has been elicited, the model will stay in that stable state and not return to the resting state, even though current injection is switched off (see inset). **(B1 inset)** Voltage response to a 2 s current pulse of 15 pA for $G_{Nap} = 2$ nS. The resting state (gray dot on the lower curve in **B1**) is destabilized at pulse onset and a plateau is elicited (blue dot on the upper curve in **B1**). At pulse offset, the plateau is maintained, even though the injected current is brought back to zero, and channel noise is not sufficient to go back to the resting state. **(B2)** Domain of bistability between quiescence and plateau (shaded) in the $I - G_{Nap}$ plane for $G_{Kdr} = 5$ nS. It is delimited by the line SN₂ where a SN bifurcation of fixed points occurs and by the subcritical Hopf bifurcation line HB where the plateau becomes unstable. Bistability requires that G_{Nap} exceeds 1.35 nS, and the domain of bistability enlarges as G_{Nap} is increased further. The two horizontal lines correspond to the two cases shown in **(B1)** $G_{Nap} = 1.65$ nS and 2 nS. **(C)** Behavior of the model when slow inactivation is incorporated. The bifurcation diagram of the basic model (without slow inactivation) for $I = 10$ pA and $G_{Kdr} = 5$ nS (same conventions as in **Figure 7B**) and the stable limit cycle (black solid curve) obtained when slow inactivation is added are superimposed. The limit cycle is comprised of four successive phases (see labels): (1) long plateau during which I_{Nap} slowly inactivates, (2) fast transition to the quiescent state, (3) repolarization episode during which I_{Nap} slowly de-inactivates, and (4) fast transition back to the plateau. Each plateau starts with a full-blown action potential followed by rapidly decaying spikelets. Note that the bifurcation HB is subcritical here (unstable limit cycle shown by dashed red curve), at variance with square wave bursting (supercritical bifurcation and stable limit cycle); this is a characteristic feature of pseudo-plateau bursting. Note also that the plateau extends beyond the bifurcation HB because it is only weakly unstable then. Responses to a 15 s current pulse are shown on the right side. Top left: voltage response ($G_{Nap} = 2.5$ nS); top right: behavior of the 'effective' conductance of the G_{Nap} channels, that is, the maximal conductance G_{Nap} multiplied by the slow inactivation variable s . Bottom left: voltage trace when channel noise is added to fast and slow gating variables; bottom right: voltage trace when G_{Nap} is increased by 50% to 3.75 nS. **(D)** Mixed events. The bifurcation diagram of the basic model for $G_{Kdr} = 5$ nS and $I = 12$ pA and the stable limit cycle obtained in the presence of slow inactivation ($G_{Nap} = 2.5$ nS) are superimposed. Here again, the limit cycle comprises four successive phases (see labels): (1) slow inactivation of I_{Nap} that leads to the crossing of the bifurcation point HB₂ and then to the destabilization of the plateau potential; (2) fast transition to the spiking regime; (3) repetitive spiking during which I_{Nap} slowly de-inactivates, which leads to the crossing of the bifurcation point SN₂ and terminates the spiking episode; and (4) fast transition back to the stable plateau potential. Response to a 15 s current pulse of 12 pA is shown on the right in the absence of any channel noise. Top: voltage trace (same labels as in the bifurcation diagram on the left); bottom: variations of the 'effective' conductance $G_{Nap}s$ (same labels as in the voltage trace). Note that de-inactivation sufficient to trigger a new plateau occurs over a series of successive spikes, hence the small oscillations visible on the trace. Note also that in **(C)** and **(D)** the first plateau lasts longer than the following ones, as in electrophysiological recordings of embryonic V1^R cells displaying repetitive plateaus. This form of adaptation is caused by the slow inactivation of the persistent sodium current.